Using Deep Learning and Multi-source Remote Sensing Images to Map Landlocked Lakes in Antarctica

Anyao Jiang[1#], Xin Meng[1#], Yan Huang[1], Guitao Shi[1,2*]

[1] Key Laboratory of Geographic Information Science (Ministry of Education), School of Geographic Sciences and State Key Laboratory of Estuarine and Coastal Research, East China Normal University, Shanghai, 200241, China

[2] Key Laboratory of Spatial-temporal Big Data Analysis and Application of Natural Resources in Megacities, Ministry of Natural Resources, Shanghai, 200241, China

[#] These authors contributed equally to this work.

Correspondence to: Guitao Shi (gtshi@geo.ecnu.edu.cn)

Abstract. Antarctic landlocked lakes' open water (LLOW) plays an important role in the Antarctic ecosystem and serves as a reliable climate indicator. However, since field surveys are currently the main method to study Antarctic landlocked lakes, the spatial and temporal distribution of landlocked lakes across Antarctica remains understudied. We first developed an automated detection workflow for Antarctic LLOW using deep learning and multi-source satellite images. The U-Net model and LLOW identification model achieved average F1 scores of 0.90 and 0.89 on testing datasets, respectively, demonstrating strong spatio-temporal robustness across various study areas. We chose four typical ice-free areas located along the coastal Antarctica as our study areas. After applying our LLOW identification model to a total of 79 Landsat-8 OLI images and 330 Sentinel-1 SAR images in these four areas, we generated high spatiotemporal resolution LLOW time series from January to April between 2017 and 2021. We analyzed the fluctuation of LLOW areas in the four study areas, and found that during expansion of LLOW, over 90% of the changes were explained by positive degree days; while during contraction, negative degree days changes accounted for more than 50% of the LLOW area fluctuations. It is shown that our model can provide long-term LLOW series products that help us better understand how lakes change under a changing climate.

1. Introduction

25   Antarctic lakes play a crucial role in the ecosystem of Antarctica and are reliable indicators of climate change (Lyons et al., 2006). These lakes can be divided into three main types: landlocked lakes, epiglacial lakes, and supraglacial lakes. Landlocked lakes, located in local depressions and usually free of ice during austral summer, primarily receive water inflow from the melting of seasonal snow cover (Shevnina et al., 2021). Epiglacial lakes are situated at the boundary between areas of rock and ice, and melting of the glacier ice is the main source of water inflow into them. Supraglacial lakes are found on the surface

30   of ice sheets, glaciers, and ice shelves, forming during the summer melt (Hodgson, 2012).

Extensive research confirms diverse microorganisms in Antarctic lakes, including prokaryotes like bacteria and eukaryotes such as phytoplankton (Parnikoza and Kozeretska, 2019; Izaguirre et al., 2021; Keskitalo et al., 2013; Rochera and Camacho, 2019). Cyanobacteria play a crucial role in primary production and nutrient cycling, as highlighted by studies on their diversity and distribution (Taton et al., 2006; Komárek et al., 2012), alongside findings on unique microbial assemblages, such as

35   Hymenobacter sp., and diverse bacterial communities (Koo et al., 2014; Huang et al., 2014; Carvalho et al., 2008; Papale et al., 2017). These studies underscore the ecological importance and high diversity of Antarctic lake ecosystems.

Antarctic lakes are rather sensitive to environmental change, especially under a warming climate (Quayle Wendy et al., 2002). Seasonally ice-covered lakes magnify the warming trends observed in air temperature (Convey and Peck, 2019). Recent studies have highlighted the impact of increased temperature and melting of snowfields and glaciers on Antarctic lakes (Izaguirre et

40   al., 2021; Stokes et al., 2019). In particular, the changes in the lake-ice and open water area can have significant implications for the lake environment, affecting both physical and biological aspects. Physically, alterations in lake-ice and open water area influence thermal stratification, leading to variations in heat distribution and vertical mixing within the water column (Preston et al., 2016; Lazhu et al., 2021). This, in turn, has implications for the biological effects observed. The occurrence peak of primary consumers (Hébert et al., 2021; Izaguirre et al., 2021), nutrient regime (Prater et al., 2022; Yang et al., 2021), the

45   development of planktonic and benthic microbial population (Camacho, 2006), and the availability of suitable oxythermal habitat for cold-water organisms (Pöysä, 2022) all can be influenced by the changes in lake-ice and open water area. Rising temperatures and stratification, coupled with reduced ice cover and increased nutrient inputs, may promote the growth of specific phytoplankton (Prowse et al., 2011). Landlocked lakes situated in coastal Antarctica typically undergo rapid species replacements during the active phytoplankton growth season, resulting in changes in plankton abundance (Izaguirre et al.,

50   2021). For example, observations in Lake Limnopolar, Byers Peninsula, have demonstrated that temperature-induced warming significantly alters carbon flow, thereby impacting the abundance of plankton in the lake ecosystem (Villaescusa et al., 2016). Over the past decade, thanks to the development of satellite remote sensing, there has been an increasing interest in the detection of Antarctic lakes. Compared to manual digitizing, automated lake detection method is more suitable for larger-scale assessments because it can be automatically applied to hundreds of satellite scenes and can avoid user bias (Arthur et al., 2020).

55   A number of methods have been developed to map Antarctic supraglacial lakes including threshold-based lake classification methods (Fitzpatrick et al., 2014; Moussavi et al., 2020), adaptive classification methods (Johansson and Brown, 2013), and

machine learning algorithms (Dirscherl et al., 2020, 2021b). Most of previous works mainly focus on the detection of supraglacial lakes (Dirscherl et al., 2021b; Dirscherl et al., 2021c; Leeson et al., 2015; Li Qing, 2021; Moussavi et al., 2020). Currently, the semi-automated algorithm has been developed for the detection of water bodies in Greenland (Miles et al., 2017).

60   This method utilized Sentinel-1 Synthetic Aperture Radar (SAR) and Landsat-8 Operational Land Imager (OLI) imagery to monitor surface and subsurface lakes on the Greenland Ice Sheet. As for Antarctic landlocked lakes, field surveys served as the primary method (Shevnina et al., 2021; Lecomte et al., 2016; Shevnina and Kourzeneva, 2017; Harris and Burton, 2010). Due to the limited study area scope and non-uniform of field surveys, the spatio-temporal distribution of landlocked lakes across Antarctica remains understudied. Unlike the identification of supraglacial lakes, the detection of landlocked lakes

65   requires information of surrounding land covers. Optical remote sensing images are disturbed by frequent clouds in Antarctica, and SAR images have difficulty capturing the information of land covers around lakes. In addition, compared to single-polarization SAR images, the utilization of multi-polarization SAR images can improve the capability to distinguish LLOW from other ground objects (Zakhvatkina et al., 2019). However, the high-resolution GRD products only provide single polarization over the Antarctic continent. The high-resolution multi-polarization SAR images are not available in Antarctica.

70   Thus, to better understand the dynamics of landlocked lakes in Antarctica, more efficient and accurate methods are needed. This study aims to apply a deep learning approach to detect the landlocked lakes' open water (LLOW) area in Antarctica in combining the Landsat 8-9 OLI and SAR imagery. Then, we aim to investigate the variations in LLOW and their relationship with environmental factors, such as temperature. To the best of our knowledge, this study represents the first attempt to map the open water area of landlocked lakes in Antarctica using remote sensing data.

75

2. Research Data

2.1 Study Area

Four typical ice-free areas distributed on coastal Antarctica were selected as study areas (Fig. 1). Antarctic Peninsula have experienced the largest increases in near-surface air temperature in the Southern Hemisphere during the past decades (Turner

80   et al., 2016). As a representative site of the Antarctic Peninsula, Clearwater Mesa (CWM; 57.71°W, 64.03°S) on James Ross Island was chosen due to its high density of lakes, unique geomorphological setting, remote elevated position, and lack of previous human presence (Roman et al., 2019). In East Antarctica, we selected two large ice-free oases, Larsemann Hills (LHs; 76.23°E, 69.41°S) and Vestfold Hills (VHs; 78.18°E, 68.58°S). The VHs is a 400 km^2 area of ice-free rock (Seppelt and Broady, 1988), while LHs is the second largest ice-free oasis along the East Antarctica with an area of about 50 km^2 (Shi et

85   al., 2018). The Schirmacher Oasis (SO; 11.65°E, 70.76°S), which is an east-west trending narrow strip, with an ice-free area of about 35 km^2 (Srivastava et al., 2013), was chosen to represent the higher latitude areas of Antarctica. Since SO is located about 100 km from the coast, it can also represent the inland area of Antarctica. In these areas, the water source of landlocked lakes is mainly from the melting of seasonal snow cover.
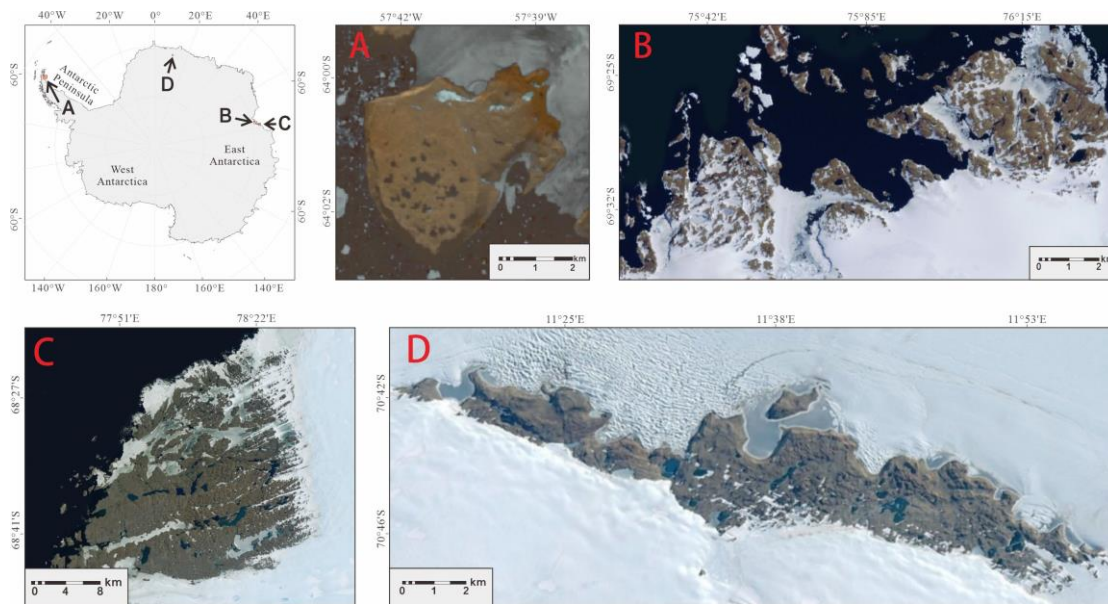
90

Figure 1. Map of study areas. Satellite images based on Landsat 8 and Esri World Imagery scenes show examples of landlocked lake occurrence. Scenes used for this figure include: (A) Clearwater Mesa (CWM; Landsat 8; 2 February 2016), (B) Larsemann Hills (LHs; Esri World Imagery; 7 April 2022), (C) Vestfold Hills (VHs; Esri World Imagery; 7 April 2022), and (D) Schirmacher Oasis (SO; Esri World Imagery; 7 April 2022).

95

2.2 Dataset

The OLI onboard the Landsat 8-9 satellite captures optical information in the visible, near infrared, and shortwave infrared portions (VNIR, NIR and SWIR), enabling the comprehensive assessment of diverse surface features. The Landsat 8-9 OLI data are superior in the enhanced radiometric capabilities and the expanded range of spectral bands (Gorji et al., 2020).
100 Leveraging the capabilities of Landsat 8-9 OLI facilitates the better monitoring of the LLOW. Thus, a total of 79 optical images of Landsat 8-9 Collection 1 with 30m resolution between January and April from 2014 to 2022 were obtained from the United States Geological Survey (USGS) Global Visualization Viewer (GLOVIS) portal (http://earthexplorer.usgs.gov/). Landsat 8-9 satellite has a 16-day repeat cycle. However, cloud cover frequently hampers the detection through visible bands within the study areas. Whenever thick layers of clouds are present above our study areas in the Landsat images, those images are
105 excluded from our study. As a result, the time interval between usable Landsat images can vary. In the Landsat OLI products, the optical bands 1-7 were utilized to identify the land cover in the study areas.

The Sentinel-1 mission is dedicated to SAR imaging and provides the all-weather, day-and-night imagery at C-band. The SAR-based landscape detection offers a distinct advantage over optical approaches by mitigating the challenges posed by cloud interference. Consequently, it can offer datasets for obtaining the long time-series monitoring of the LLOW. Because of the

110   advantages of SAR images, Sentinel-1 datasets had been widely used for Antarctic open water and snowmelt detection studies (Bowden et al., 2006; Liang et al., 2021; Dirscherl et al., 2021c). European Space Agency (ESA) facilitates access to various Sentinel-1 products, including raw level-0 data, processed level-1 Single Look Complex (SLC) data and level-1 Ground Range Detected (GRD) data. To accurately determine the peak dates of landlocked lake area changes, the temporal resolution of area measurements needs to be at the weekly or daily time scale. Considering the high temporal resolution requirement of LLOW

115   detection tasks, we used a total of 330 high-resolution Sentinel-1 SAR images from the Interferometric Wide (IW) Swath GRD products with about 10-m pixel space, which were acquired from Alaska Satellite Facility (ASF) (https://search.asf.alaska.edu/). All Sentinel-1 images are from the descending orbit, in order to avoid geometric distortions and orthorectification limitations (Wangchuk et al., 2019). These selected Sentinel-1 images for CWM, LHs and VHs span from 2017 to 2021. However, for SO, where Sentinel-1 images are unavailable prior to 2019, only the images during 2020 and 2021 were obtained. The revisit

120   period of Sentinel-1 satellites is 12 days. By utilizing both Sentinel-1A and Sentinel-1B images, we obtained a shorter time interval of 6 days between consecutive Sentinel-1 images. These GRD products play a critical role in distinguishing the LLOW in the study areas.

Our dataset of wind speed for four areas and daily mean near-surface temperatures for CWM and SO came from ERA5-land dataset obtained from Google Earth Engine (Muñoz Sabater, 2019). The daily mean air temperatures for LHs and VHs were

125   derived from the weather stations at Zhongshan Station (Ding et al., 2022) and Davis Station. Hereafter, we used "temperature" to represent "daily mean air temperature" and "daily mean near-surface temperature". To facilitate the terrain correction, we employed the Copernicus 90 m Global DEM data.

During the Antarctic summer, the snow cover on the lake surface undergoes melting, and consequently the LLOW will be present, which can be easily observed through remote sensing technique. The melting and freezing processes typically occur

130   between September and April. However, the identification of LLOW is challenged by rising temperature events during September and December. These occasional temperature increases can trigger the relatively high temperatures, and increased snow wetness. This wetness increase can reduce the backscatter of the snow surface (Shokr and Dabboor, 2020). The events lead to the lower backscatter of both snow and snow-covered ice, resulting in similar backscatter characteristics among ice, snow, and LLOW. During the melting period of landlocked lakes, which in general spans from September to December, frozen

135   landlocked lakes may be covered by wet snow due to rising temperature events, resulting in low backscatter. Consequently, these frozen lakes are not LLOW but incorrectly identified as LLOW. During January to April, the melt landlocked lakes have less snow cover and are less affected by the rising temperature events. Thus, the identification of LLOW from January to April is much more accurate compared to September to December. To evaluate the influence of rising temperature events from September to December, we sampled pixels of open water, land ice layers and sea ice layers from several SAR images during

140   this period. We also sampled LLOW pixels in January as the reference for backscattering analysis. We found that the backscatter of sampled land ice layers was as low as that of sampled LLOW in January in our study areas (Supplementary Table 1). Consequently, our model cannot effectively distinguish between LLOW and ice layer in these images from September

to December. Our analysis focuses on the changes in LLOW from January to April, when the identification accuracy is relatively high.

145 To train and validate the U-Net and the random forest (RF) model, we manually annotated ground truth labels from Landsat 8-9 OLI images and Sentinel-1 images. For the U-Net model, several Landsat images were selected, and the pixels in the images were annotated as "open water", "ice", and "rock" to serve as ground truth. To enhance the classification capability of U-Net in various scales, the side lengths of Landsat images ranged from 30 pixels to 200 pixels. We annotated 23 patches with 17100 pixels for U-Net. For the RF model, directly annotating the ground truth in SAR images is challenging and time-

150 consuming, primarily due to their complex backscatter characteristics. Therefore, we conducted visual interpretation for Sentinel-1 images with the assistance of Landsat images (Liang and Liu, 2020). To ensure that the Landsat images represent the surface of Sentinel-1 images, we selected the Landsat and Sentinel-1 images with the closest dates. Due to the limited availability of cloud-free Landsat images, we used all cloud-free Landsat images from 2017 to 2021 to generate the sample "open water" and "others". In addition, to validate the accuracy of LLOW identification, we also annotated these Sentinel-1

155 images as "LLOW" and "others". We annotated 46 patches with the 300*300 size to train the RF model and validate the model accuracy. The 46 patches were randomly sampled at a 10% ratio to generate a sample point set. These points were then randomly divided into 80% for training and 20% for testing to train and test the RF model. Additionally, we identified the LLOW with the 46 patches and then calculated the accuracy, F1 score, and mean IoU to evaluate the identification accuracy.

160 **3. Lake open water identification**

The automated detection workflow for LLOW can be divided into three steps (Fig. 2): (1) pre-processing of Landsat and Sentinel input images, (2) open water identification, and (3) post-processing of extracted open water to generate the LLOW time series. To assess the accuracy of our LLOW detection workflow, we conducted a comparison between the identified LLOW and the labelled ground truth.

165
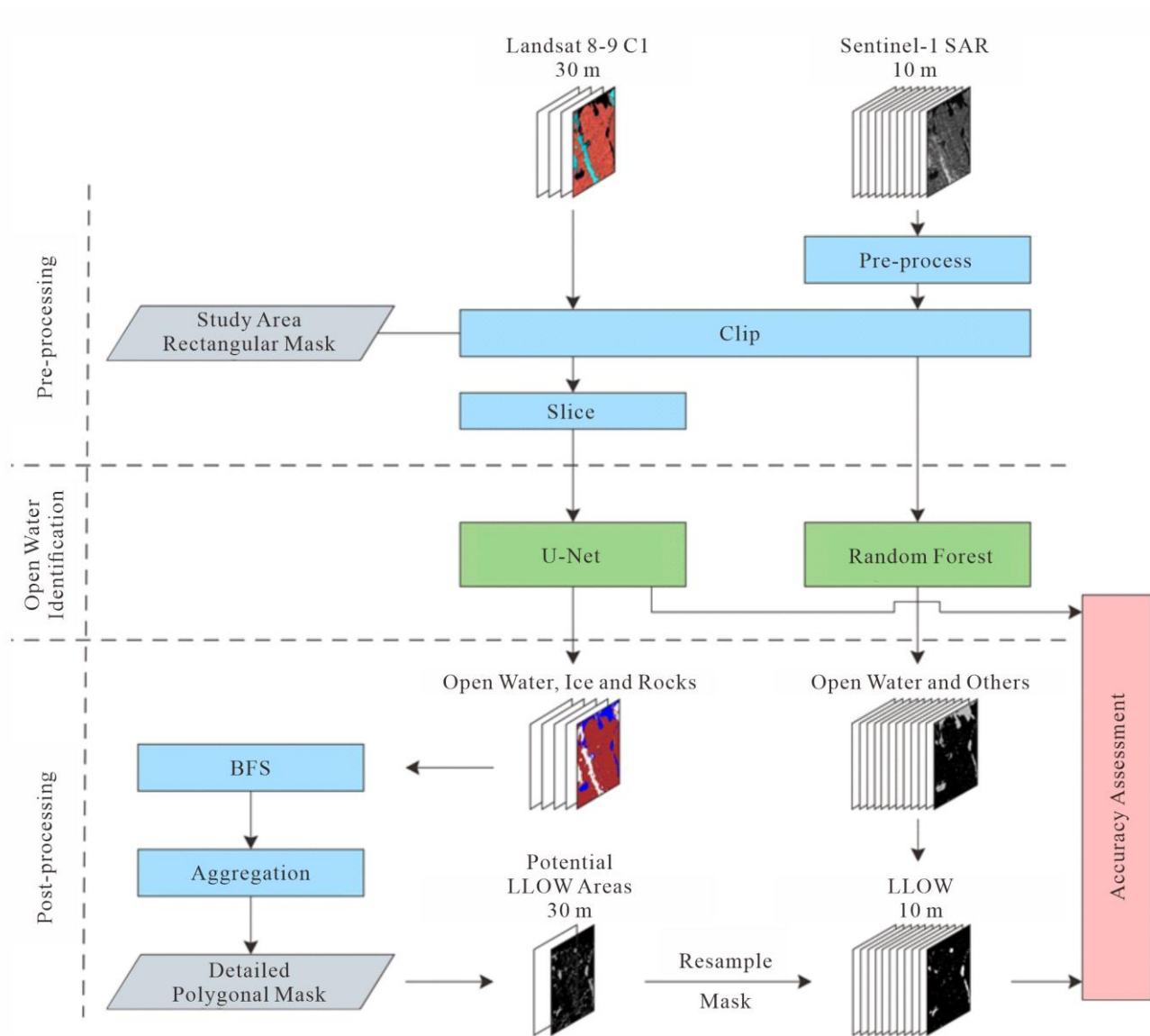
Figure 2. Workflow for detecting the landlocked lakes' open water (LLOW) in Antarctica.

3.1 Pre-Processing

170   Ensuring consistent relative location of the study area in each image enhances the comparability of the detected LLOW within the study area across different images. To achieve this, the predefined rectangular boundaries were established based on projected coordinates. We cropped images to fit within these specific boundaries, thereby unifying the relative location of the study area in the predefined boundaries. For Landsat images, we utilized the specified coordinates to apply the resampling

technique with Nearest Neighbor (NN) algorithm and perform image cropping. For Sentinel-1 images, we performed orbital correction, thermal noise removal, radiometric calibration, speckle filtering, terrain correction, and decibel conversion on the Sentinel-1 Level-1 GRD products using ESA's Sentinel Applications Platform (SNAP) software. In addition, the incidence angles in SAR images were also extracted using SNAP. Then the corrected Sentinel-1 images were then reprojected and cropped to align with the spatial extent of the cropped Landsat images.

It is necessary to expand the sample set using data augmentation to prevent the network from overfitting. Consequently, we augmented the annotated 23 sample images 20 times and obtained a total of 483 sample images. Our data augmentation methods include mirroring, translation, and rotation. Mirroring consists of three scenarios: vertical mirroring, horizontal mirroring, and vertical and horizontal mirroring. The translation involved a four-way translation up to 1/10 of the side length. The range of rotation angle was 0°-360°. Any void pixels that arose after data augmentation were filled by the reflecting adjacent image pixels. Among the 483 sample images, 80% were randomly assigned as the training set and the remaining 20% as the validation set.

The use of an overlap-tile strategy for splitting large images into smaller patches has proven effective in overcoming GPU limitations (Ronneberger et al., 2015). Thus, this strategy was employed before using Landsat images in the U-Net. We sliced the input images to the patches of 300*300 pixels. There are many small LLOW distributed across the four study areas, especially in LHs and VHs, while the U-Net is not ideal for recognizing small-scale open water. Therefore, we resampled the patches with NN from 300*300 pixels to 1024*1024 pixels, in order to magnify the small open water area. After land-cover classification using U-Net, we again resampled these classified results of 1024*1024 pixels to 300*300 pixels with NN. To reduce the border effect caused by U-Net (Dirscherl et al., 2021a), we only remained the result of 250*250 pixels in the center of the patch while discarding the edge with a length of 25 pixels.

3.2 Open Water Identification

U-Net neural network is a deep learning network for semantic segmentation based on a fully convolutional network (Ronneberger et al., 2015), which is faster to train due to its context-based learning approach (Siddique et al., 2021). In addition, it does not require the explicit specification of the input image size for achieving end-to-end semantic segmentation. For LLOW detection, U-Net network can effectively fuse the spatial and spectral information. U-Net can process the spectral information for land-cover classification, while it can also consider the spatial contexts to effectively reduce the interference of shadows and clouds. Thus, we implemented a U-Net model to detect open water in Landsat images and classify the pixels into three types of land cover: ice, open water, and rock. The backscattering distributions of ice and rock are similar in single HH polarization, so we only classified the pixels of Sentinel-1 images into two types: open water and others.

U-Net consists of an encoder and a decoder (Fig. 3). The encoder and decoder are both mainly composed of double-conv layers, which contain double convolutional layers and are used to enhance model depth (Wu et al., 2020). In the double-conv layers, batch normalization layer and the Leaky Rectified Linear Unit (LeakyReLU) layer are added to re-correct the data distribution

and achieve nonlinear computation. To avoid gradient vanishing and facilitate the deepening of the U-Net model network, we added a residual layer between the double-conv layers.
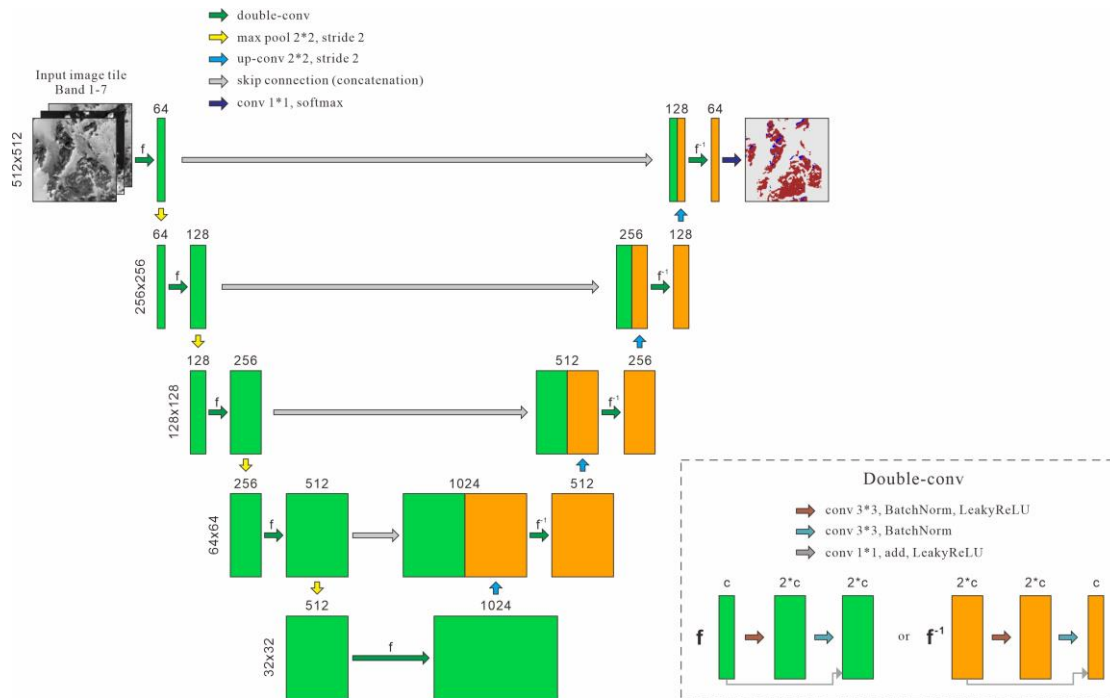
Figure 3. The structure of U-Net and double-conv layer. The numbers on the left of double-conv blocks represent the image sizes. The number above the double-conv blocks represent the feature channels after each operation. Double-conv blocks are able to double the feature channels in encoder, while they halve the feature channels in decoder.

Open water bodies exhibit a smooth surface, resulting in weaker backscatters, while areas with rougher surfaces generate stronger backscatters. The backscatter of surface varies across different incidence angles of SAR images (Wakabayashi et al., 2019). Thus, open water and other features can be distinguished based on backscatter and incidence angles. The RF model, a nonlinear modelling tool, can accurately predict and has a high tolerance to noise and outliers (Huang et al., 2021). We established the RF model for each study area to identify the open water in SAR images according to backscatter and incidence angles.

3.3 Post-processing

A landlocked lake is a water region surrounded by a rock region. Not all "open water" pixels extracted through the open water identification models are LLOW, such as glacial rivers and melted water from coastal glaciers. Besides, LLOW may be indirectly surrounded by rocks. For example, LLOW may be enclosed by ice, which in turn is surrounded by rocks. In our classified results, a classified Landsat image consists of a connected non-rock area and interspersed rock areas containing

LLOW. The BFS algorithm has been proven to be effective in removing the connected areas (Silvela and Portillo, 2001). Thus, the BFS algorithm can effectively eliminate the connected non-rock area while retaining the rock areas. BFS simulates the spreading of seawater in the Antarctic summer and leaves only rock areas where stable LLOW may exist. The supraglacial lakes, epiglacial lakes, and seawater are all removed during BFS. Finally, all the remaining open water pixels derived from Landsat images are extracted and marked as "LLOW".

The use of Landsat images in the visible and near-infrared bands is significantly hindered by cloud interference, especially along the Antarctic coast. As mentioned in Section 2.2, within the four study areas over 2014-2022, only a total of 79 Landsat images are suitable for LLOW detection. Therefore, the number of Landsat images with low cloud cover in the study areas is insufficient for our time series analysis. To improve the temporal resolution of LLOW time series, we used Sentinel-1 SAR images as supplements. SAR images are not affected by clouds but have limited spectral information and lack accuracy in distinguishing ground objects among open water, rocks, and ice. The open water identified solely from SAR imagery often includes substantial amounts of mountain shadows and lakes which were not surrounded by rocks. Without spatial information of rocks and ice, BFS algorithm is invalid to extract LLOW from open water. Consequently, SAR images only enable the identification of open water instead of LLOW. Using data from either Landsat 8-9 or Sentinel-1 alone cannot precisely capture the temporal variation of LLOW. However, combining the maximum lake area derived from Landsat with the results obtained from SAR images provides a better approach to achieve higher temporal resolution and more accurate results (Miles et al., 2017). Thus, for each study area, we defined the pixels that are classified as LLOW in multiple Landsat results as potential LLOW. Specifically, if a pixel was identified as LLOW two or more times from 2014 to 2022, it was considered as a potential LLOW pixel. We aggregated all LLOW distribution images and obtained one potential LLOW area for each study area. According to the annotated sample set, some LLOW areas are not within the potential LLOW area range. To leverage the resolution advantage of Sentinel-1 and its potential for LLOW identification, we established a buffer zone for the potential LLOW area (Wangchuk et al., 2019). As shown in Figure S1, the rate of decrease in the ignored LLOW area diminishes as the buffer radius increases. We selected a buffer radius of 20 m, where the reduction in LLOW area is most significant, and resampled the potential LLOW area into a 10-m resolution. After that, we combined the Landsat and Sentinel images, using the potential extents of LLOW and the open water derived from SAR, to generate the long-term series of LLOW.

Because previous cropped images had wide rectangular boundaries, they still retained large non-research areas. To ensure consistency of the extracted LLOW in study areas, we delineated the more detailed coordinate boundaries according to the irregular shapes of study area. Then, the detailed boundaries were used to narrow down potential LLOW regions. It is important to note that identifying LLOW in SAR images can be challenging due to various factors, such as strong wind, floating thin ice layers, and sensor speckle noise (Dirscherl et al., 2021b). These factors can impact the backscatter of LLOW and make accurate detection of LLOW difficult. For instance, congealed ice generates large bubbles, and the bubbles entrained within ice layer enhance backscatters (Hirose et al., 2008). Consequently, LLOW covered by only a few floating ice layers or affected by strong winds may exhibit higher backscatter coefficients and cannot be detected by our threshold segmentation model. Instances of strong winds and floating ice have temporary effects on the entire study area and result in significant

underestimation of LLOW. Therefore, we disregarded those underestimated LLOW results and generated a total of 285 long term-series images of LLOW. The LLOW series combined Landsat and Sentinel images have a spatial resolution of 10 m and a time resolution of ~ 6 days.

3.4 Accuracy Assessment

The accuracy of classification models is estimated by confusion matrix, accuracy, F1 score, and mean IoU. The formulas are presented in Eqs. (1), (2), (3), (4), and (5).

$$\text{Accuracy} = \frac{\text{TP}}{\text{TS}} \tag{1}$$

$$\text{F1} = 2 * \frac{\text{Precision} * \text{Recall}}{\text{Precision} + \text{Recal}} \tag{2}$$

$$\text{Precision} = \frac{\text{TP}}{\text{TP} + \text{FP}} \tag{3}$$

$$\text{Recall} = \frac{\text{TP}}{\text{TP} + \text{FN}} \tag{4}$$

$$\text{mIoU} = \frac{1}{N} \sum_{i=1}^{N} \frac{TP_i}{TP_i + FP_i + FN_i} \tag{5}$$

where N is the number of categories; TS is the total number of samples; TP is the number of true positive classified results; FP is the number of false positive classified results; TN is the number of true negative classified results; and FN is the number of false negative classified results in confusion matrix.

4. Results

4.1 Classification Results

Figure 4 illustrates the process and intermediate results involved the LLOW identification. The Landsat images were accurately classified into open water, ice, and rocks through the use of U-Net (Figs. 4e, 4f, 4g, and 4h). Compared to the images of false color band combination, the results derived from threshold segmentation contained large amounts of errors (Figs. 4m,4n,4o, and 4p). For example, the smooth ice layers were misidentified as open water in Fig. 4p. However, we obtained the information

of potential LLOW areas through the results of U-Net. To rectify these errors, the mask of potential LLOW areas were employed (Figs. 4q, 4r, 4s, and 4t), significantly improving the accuracy of LLOW identification based on SAR images.
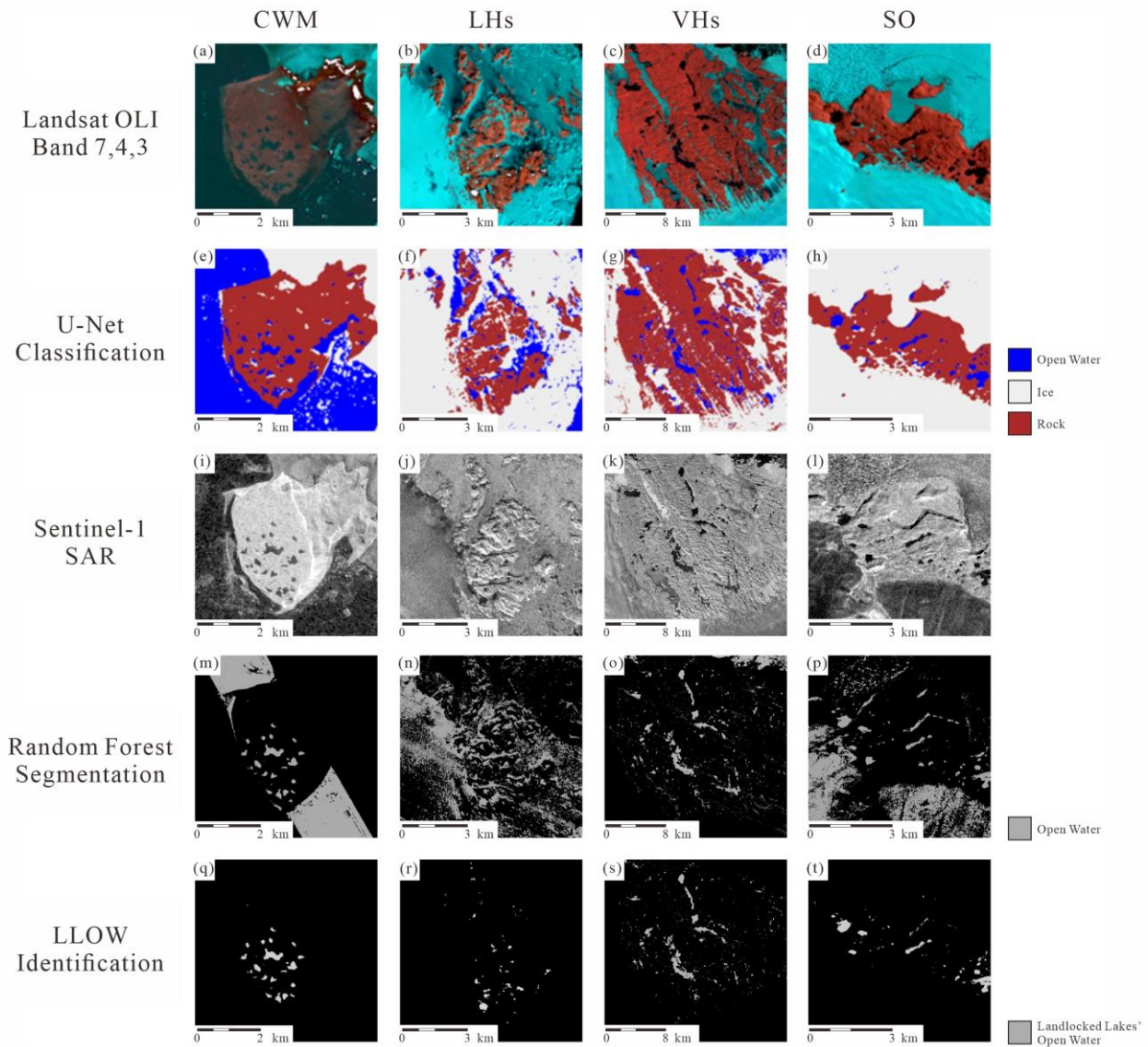
 Figure 4. The intermediate images and results in the workflow of landlocked lakes' open water (LLOW) identification. The first row displays the Landsat images by the false color band combination 7-4-3 (RGB). The white regions in these images represent the void data in band 7, 4 or 3. The second row exhibits the classification results of U-Net. The third, fourth and fifth rows represent the Sentinel images, the results of threshold segmentation, and the results of detected LLOW, respectively.

290 Figure 5 shows the classification results obtained by U-Net for extracts from all Landsat test scenes. The U-Net network has generally shown good recognition performance across various terrains in all 4 study areas. In specific, it effectively mitigates the impacts of diverse brightness and contrast levels in VHs (Figs. 5a and 5b). Moreover, it accurately distinguishes mountain shadows from water bodies in LHs without any misclassification (Figs. 5c and 5d). Notably, in SO, the presence of ice undulations causes numerous shadows. U-Net correctly identifies these shadows as ice (Fig. 5e), which can be a challenging

295 task when using threshold methods. In addition, in both the SO and CWM, there are partially melted lakes primarily composed of ice, which appears grayish (Figs. 5e and 5f). U-Net successfully identifies these lakes as ice surfaces, preventing any overestimation of open water areas.
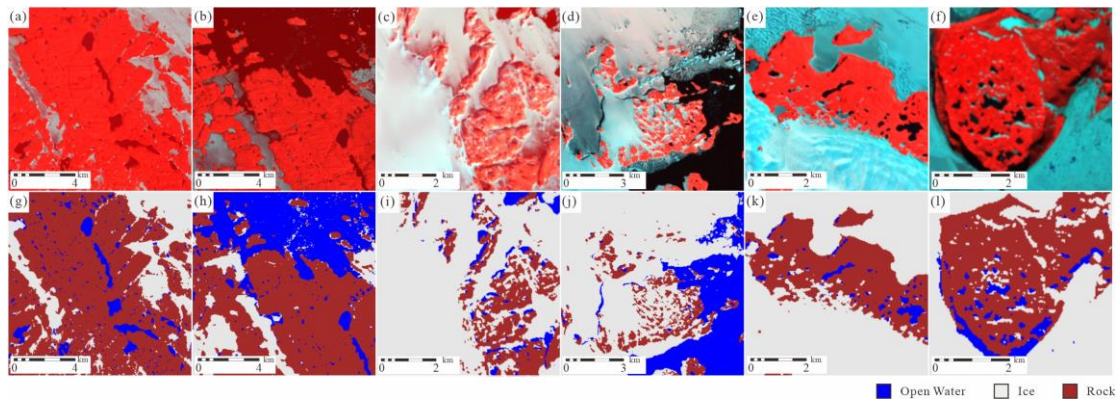
300 **Figure 5. Comparison between the Landsat images and auto-generated classification examples of U-Net. The upper row displays Landsat-8 images, using the false color band combination 7-4-3 (RGB), to enhance feature distinction. The lower row shows the corresponding auto-generated classification results of U-Net. Panels (a) and (b) represent Vestfold Hills (VHs); panels (c) and (d) represent Larsemann Hills (LHs); panel (e) represents Schirmacher Oasis (SO); and panel (f) represents Clearwater Mesa (CWM).**

305 Figure 6 displays LLOW results obtained through the fusion of Landsat and SAR images. A comparison within each row highlights differences between varied areas. For example, SO, the highest latitude area, appears completely frozen in April (Fig. 6h), while the lower latitude areas like CWM still exhibit LLOW during the same month (Fig. 6e). By contrasting the upper row with the lower row, temporal differences can be observed within the same area, where lakes show larger open water areas in the relatively warmer month of February (e.g., Figs. 6d and 6h).

310
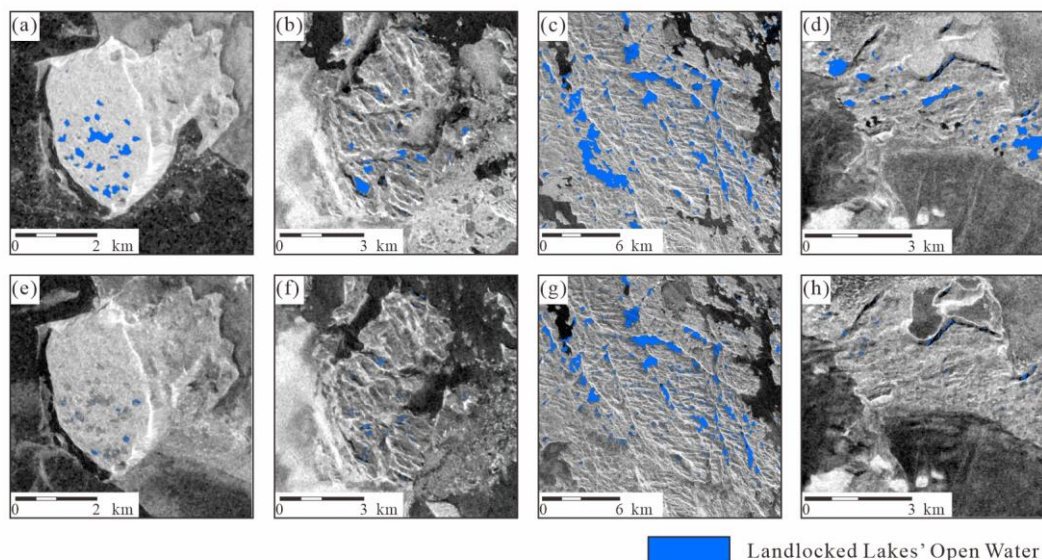
Figure 6. The landlocked lakes' open water (LLOW) area changes over time obtained through the fusion of Landsat and SAR images. The upper row shows the LLOW results in February, with lower row representing in April. Panels (a) and (e) represent Clearwater Mesa (CWM); panels (b) and (f) represent Larsemann Hills (LHs); panels (c) and (g) represent Vestfold Hills (VHs); and panels (d) and (h) represent Schirmacher Oasis (SO).

4.2 Model Validation

We compared the accuracy of LLOW identification between results obtained before applying the potential LLOW areas mask and those obtained after applying the mask in LHs (Fig. 7). Prior to applying the mask, the RF model identified a large number of false LLOW instances in low backscatter pixels. The LLOW identification only based on SAR images resulted in a mIoU value of only 0.29 when compared to the ground truth labels. However, the masking process based on potential LLOW areas successfully reduced the majority of false LLOW instances and improved the mIoU value to 0.74. The increase in the mIoU suggests that masking using potential LLOW areas can compensate for the lack of spectral information in Sentinel-1 images, thereby enhancing the accuracy of the LLOW identification model.
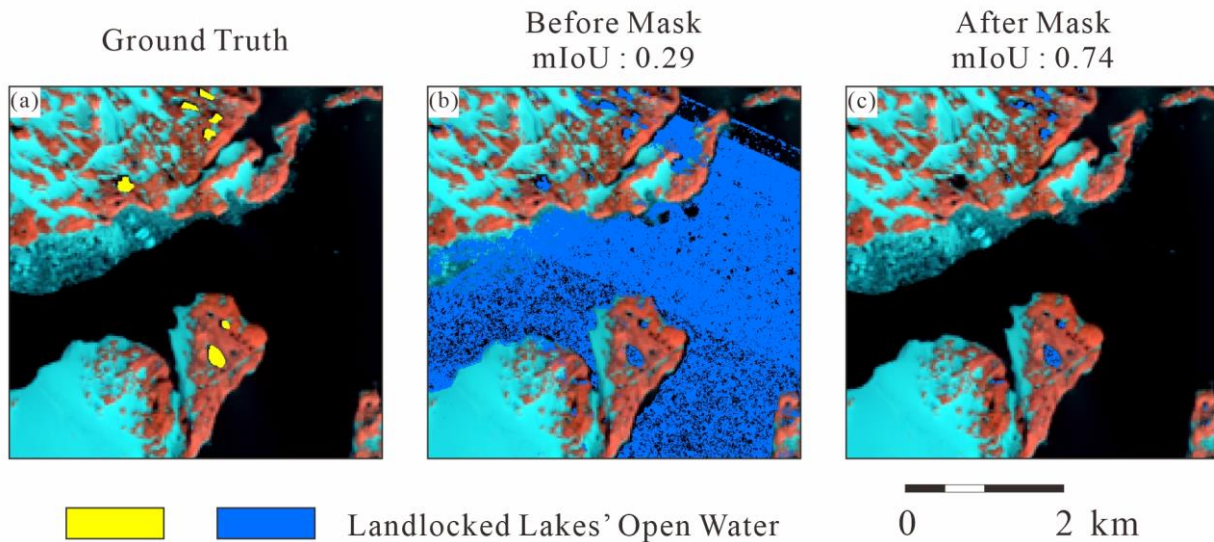
Figure 7. Accuracy comparison of LLOW identification before and after mask in LHs. The background images are displayed from false color combination of 7-4-3 bands. The result before mask was derived from threshold segmentation.

Our land-cover classification model, based on U-Net, has achieved the average accuracy, F1 score, and mIoU values of 0.93, 0.90, and 0.82, respectively, on the test datasets, indicating the reliable and accurate classification of land cover. The LLOW identification model yielded the mean accuracy, F1 score, and mIoU values of 0.94, 0.89, and 0.81, respectively, for four study areas on the test set. We further validated the model performance on four test patches (Fig. 8). The LLOW identification model yielded the F1 scores ranging from 0.88 to 0.95 and mIoU ranging from 0.81 to 0.90. Among the four areas, SO exhibited the highest mIoU value of 0.90, suggesting the most similar spatial distribution between the predicted LLOW and the ground truth. LHs showed the lowest mIoU of 0.81, while CWM and VHs showed the mIoU values of 0.82 and 0.83, respectively. In VHs and SO, the locations and areas of LLOW were well recognized (Figs. 8k and 8l). In LHs, the spatial distribution of LLOW was also accurately detected, although there were some inconsistencies in the boundaries between the ground truth and the predicted lakes (Fig. 8j). In addition, in CWM, the model successfully identified all LLOW areas, but it misclassified the areas covered by floating ice with low backscatter (Fig. 8a) as LLOW. Overall, our model demonstrated proficiency in detecting LLOW areas, providing reliable information on the spatial distribution and extent of LLOW.
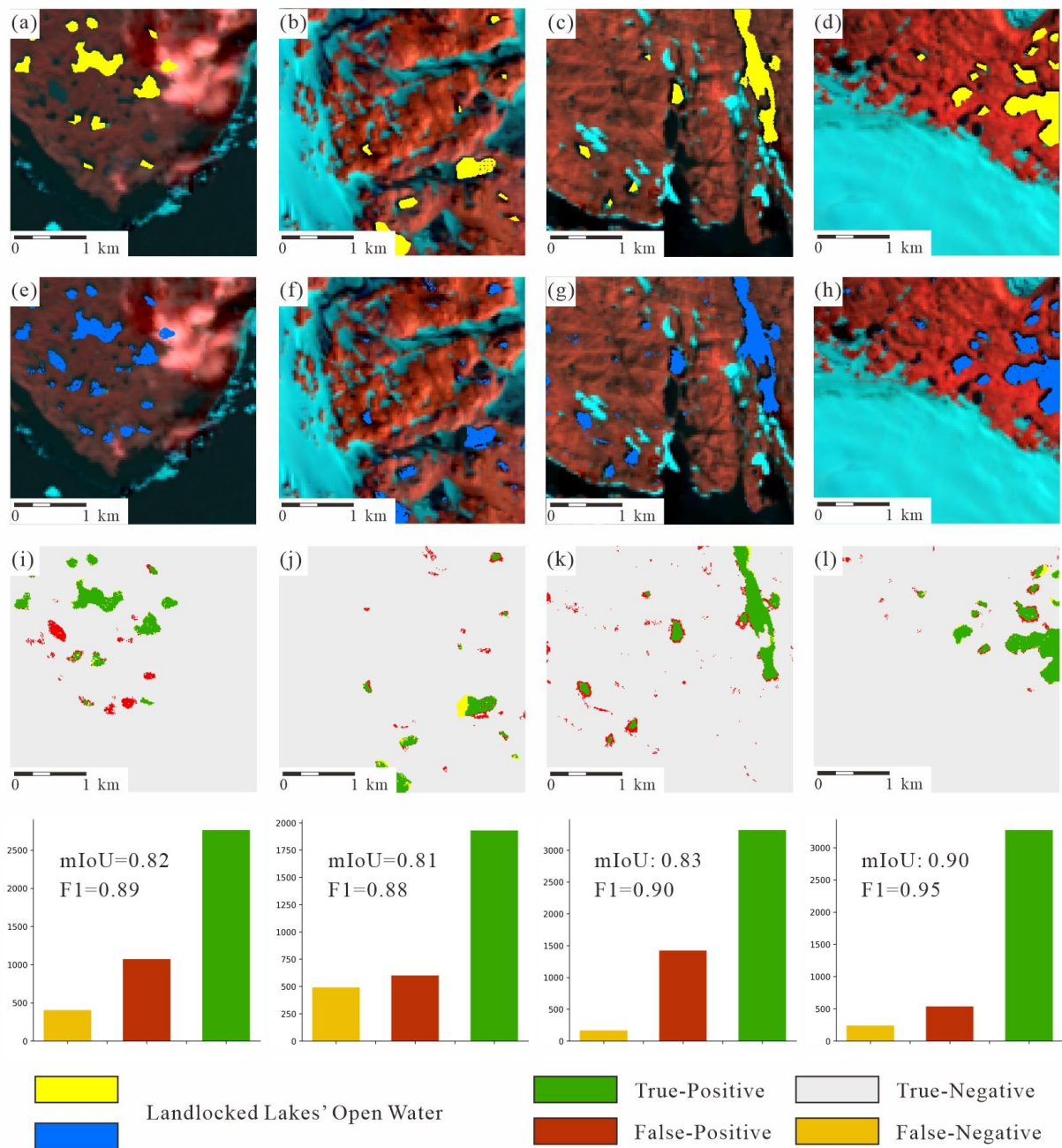
Fig 8. Validation of landlocked lake identification model in testing dataset for four areas. The four columns of images are validation images for CWM, LHs, VHs and SO. The first, second, and third rows are ground truth, predicted, and spatial errors images, respectively. The background images are displayed from false color combination of 7-4-3 bands. The spatial distribution of classification errors is obtained from overlapping ground truth and predicted images.

345

4.3 Seasonal variations in LLOW area

The study focused on changes in LLOW from January to April across four different areas in Antarctica. Figure 9 presents the
350   spatial and temporal variations of LLOW area during the study period. Our results indicate an initial increase followed by a decreasing trend in the overall LLOW area. Notably, the occurrence and duration of maximum LLOW areas varied among study areas, with the highest value observed in early January in CWM, while the inland Antarctica SO experienced its peak LLOW area at the end of January, lasting for less than two satellite revisit cycles (12 days). The rate of decrease in LLOW area slowed down from late March, approaching a relatively stable low-value stage. By April, the LLOW areas had reduced
355   to approximately 20% of their maximum value for CWM, while the LHs and SO at higher latitudes decreased to 10% of their maximum or approached zero.

In addition to seasonal variations, interannual variations in LLOW area were observed. For example, LHs exhibited significant variation in LLOW areas in different years, with the maximum recorded in 2018 being only 60% of that in 2019 (Fig. 9b). Furthermore, CWM experienced a significant freezing and thawing process in March 2017, when the LLOW area dropped to
360   less than 50% of its maximum before subsequently rebounding to the maximum value (Fig. 9a).
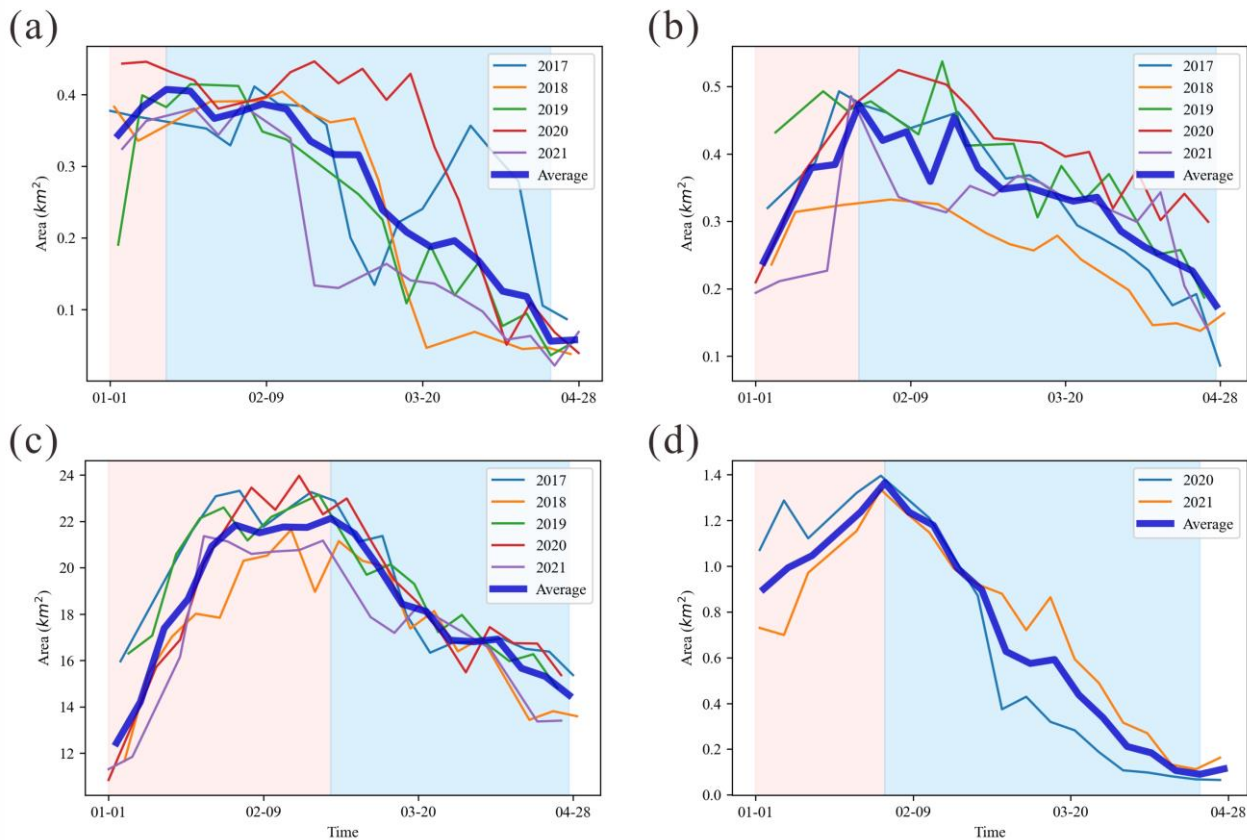
365

5. Discussion

The changes in LLOW area can be categorized into two distinct phases: the growth phase and the decline phase (Figure 9). The growth phase spans from the initiation of our data collection until reaching the maximum LLOW area, while the decline phase extends from the maximum area to the minimum area after reaching the peak. In the following sections, we will discuss
370   these two phases separately.

5.1 Growth phase of LLOW area

With the onset of austral summer, lake surface ice and snow melt, resulting in the generation of meltwater, which contributes to an increase in the LLOW area. This process is closely associated with the changes in temperature, especially the occurrence
375   of days with temperatures exceeding 0°C (Braithwaite and Hughes, 2022; Li Qing, 2021; Wake and Marshall, 2015; Maisincho et al., 2014; Barrand et al., 2013; Johansson et al., 2013). Thus, we evaluate the positive degree-day sum (PDD), which represents the cumulative sum of temperatures above the melting point during a specific period (Cogley et al., 2010). In this study, the PDD for a given day is calculated as the sum of temperatures exceeding 0°C from November 1st of the previous year until the current day. It is important to note that we only analyzed the PDD for LHs and VHs in this study, considering
380   that the automatic weather station (AWS) data are only available at the two sites. The PDD is calculated using the Eq. (6):

$$PDD_n = \sum_{i=0}^{n} \begin{cases} T_i, & T_i > 0 \\ 0, & T_i \leq 0 \end{cases} \tag{6}$$

Here, the positive degree-day sum prior to the day n is denoted as PDD_n (°C) and T_i represents the station mean temperature (°C) measured on day i. Fig. 10 illustrates the relationship between PDD and LLOW area change over time in LHs and VHs. During the growth phase of the LLOW area, the average R^2 value is around 0.9, indicating that PDD can explain ~90% of the increase in LLOW area. However, there was a notable exception in LHs in 2019, characterized by an unusual cooling event
385   from mid to late January. This event persisted for several consecutive days with temperatures below 0°C, resulting in a decline in the LLOW area. In addition, since the LLOW area had already reached its maximum at the beginning of January in LHs in 2018, the growth phase was short and less discernible, leading to a lack of significant correlation between PDD and the LLOW area.

PDDs can also influence the year-to-year fluctuations in LLOW area, but the relationship between changes in PDD and LLOW area is non-linear. For instance, the maximum PDD in 2017 was more than 2 times higher than that in 2018 in LHs, yet the
390   maximum area increased by 50% (Figs. 10a and 10b). The maximum area of VHs remains relatively stable over the 5 years.

When PDD reaches a certain threshold, all LLOW areas have already melted, so further increases in PDD do not lead to changes in LLOW area. Therefore, across different years, significant differences in PDD can result in minimal variation in LLOW areas. Based on this, it can be inferred that the threshold for PDD in LHs is likely between 25°C and 35°C. When PDD exceeds 35°C, the maximum LLOW area keeps relatively invariant at ~ 0.5 km^2.
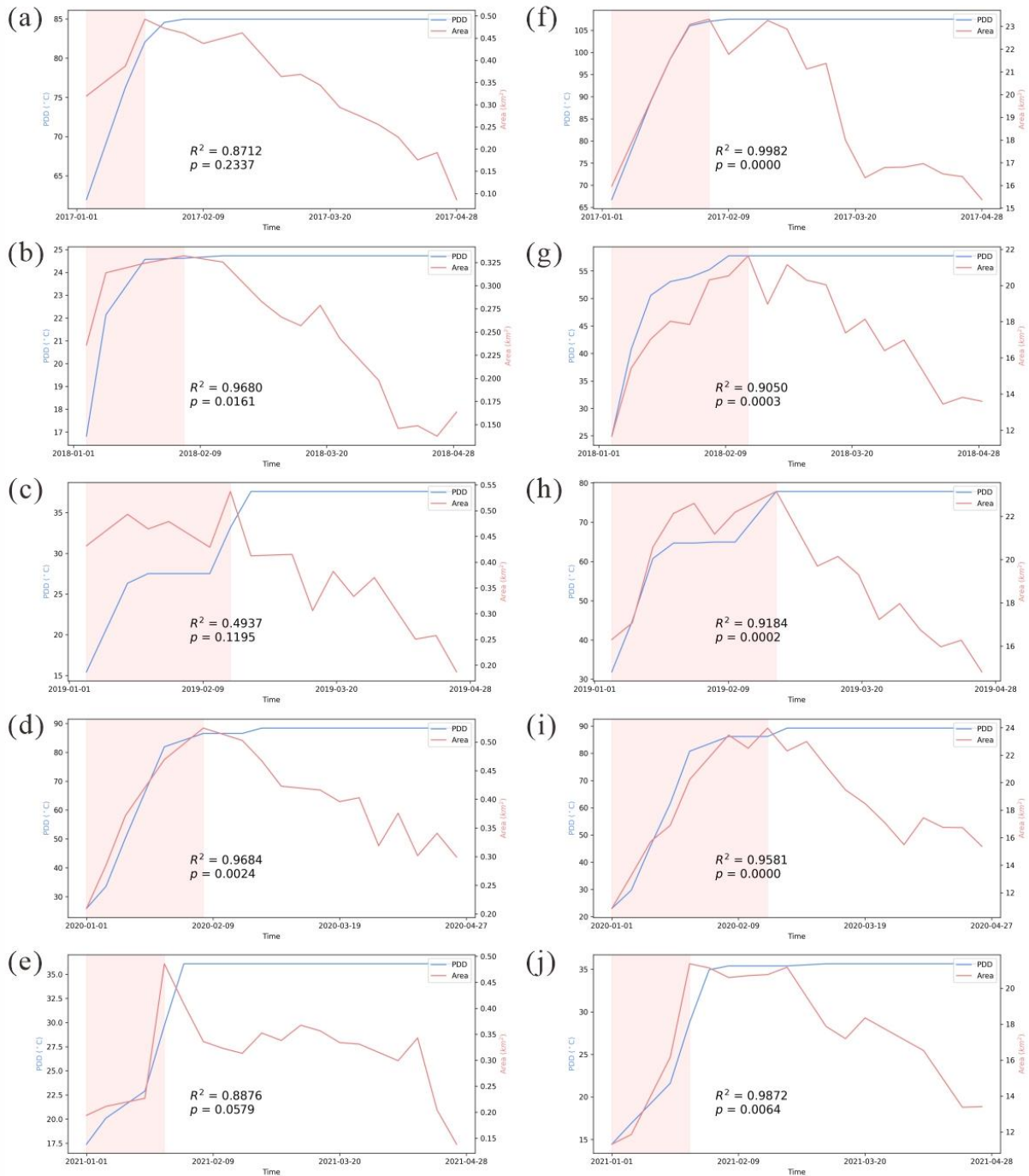
Figure 10. The positive degree-day sums (PDD) and landlocked lakes' open water (LLOW) area change during the 2017 (a), 2018 (b), 2019 (c), 2020 (d), and 2021 (e) melt seasons in Larsemann Hills (LHs) and during the 2017 (f), 2018 (g), 2019 (h), 2020 (i), and 2021 (j) in Vestfold Hills (VHs). In the figure, the red interval represents the growth phase of LLOW area The R² value in the figure is calculated from a linear fit of PDD and LLOW area during the growth phase.

400

5.2 Decline phase of LLOW area

405 Cumulation in successive negative air temperature days contributes to the lowering of water temperature and the commencement of the water freezing process, i.e., the formation and longer-term persistence of ice cover (Graf and Tomczyk, 2018). Therefore, we calculate the negative degree-day sum (NDD) by using Eq. (7), which represents the cumulative sum of temperatures below the melting point during a specific period.

$$NDD_n = \sum_{i=0}^{n} \begin{cases} T_i, & T_i < 0 \\ 0, & T_i \geq 0 \end{cases} \tag{7}$$

Here, the negative degree-day sum prior to the day n is denoted as NDD_n (°C) and T_i represents the station mean temperature
410 (°C) measured on day i. The relationship between the LLOW area and NDD in each area during the freezing season is significant (Table 1). The calculation of the R^2 value was based on a linear fit of the NDD and the LLOW area, ranging from the maximum LLOW area to the minimum. In all four study areas, the R^2 values were found to be greater than 0.5. This indicates a strong response of the LLOW area to NDD changes during the decline phase of the LLOW area.

415 **Table 1. R^2 of the LLOW area and negative degree days in the freezing phase between 2017 and 2021.**

Year	CWM	LHs	VHs	SO
2017	0.52[**]	0.95[**]	0.72[**]	
2018	0.84[**]	0.94[**]	0.85[**]	
2019	0.73[**]	0.75[**]	0.82[**]	
2020	0.88[**]	0.85[**]	0.78[**]	0.78[**]
2021	0.57[**]	0.59[**]	0.86[**]	0.97[**]
Average	0.71	0.82	0.81	0.88

* p < 0.05, ** p < 0.01.

The relationship between the LLOW area and NDD in CWM in 2017 exhibited a relatively low R^2 value (0.52). During that year, sharp declines and subsequent rebounds of the LLOW area were observed (Fig. 11). As temperatures plummeted, the
420 LLOW area decreased rapidly, nearly reaching its nadir simultaneously. Conversely, with rising temperatures, the LLOW area responded promptly, highlighting temperature's predominant influence on fluctuations in the LLOW area. Therefore, using NDD instead of temperature to explain variations in the LLOW area during the freezing phase may overlook these instances of temperature-driven rebounds during decline phase.
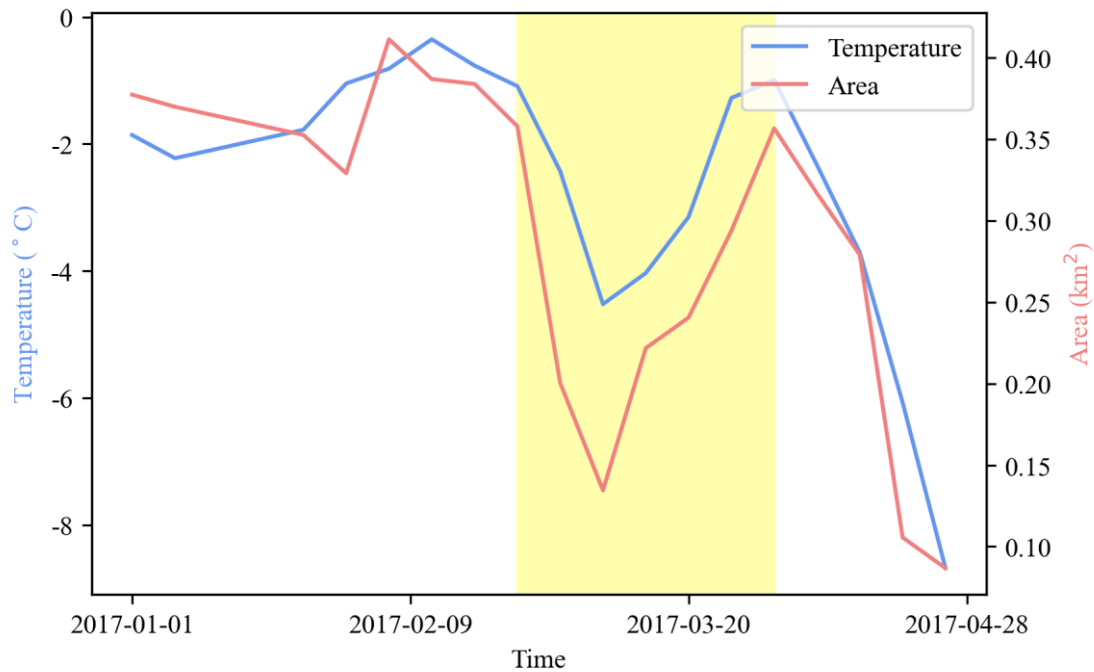
425

Figure 11. The temperature and the landlocked lakes' open water (LLOW) area in CWM in 2017. The yellow interval represents the declines and rebounds of lake area and temperature.

During the freezing stage, the depth of a lake will affect the time of lake ice formation (Kirillin et al., 2012), which in turn

430   affects the reduction in LLOW area. Shallower lakes tend to lose heat more quickly, leading to earlier ice cover formation. In contrast, deeper lakes possess greater heat capacity, resulting in a slower cooling process and delayed ice formation. For instance, VHs and LHs are close to each other with similar temperature conditions, so the LLOW area should begin to decrease around the same time. However, in LHs, the LLOW area started to decrease continuously from late January, approximately one to two weeks earlier than in VHs. This discrepancy may be attributed to the fact that the average lake depth in VHs is ~

435   30 m, with some lakes exceeding ~100 m in depth, whereas LHs consist of lakes with an average depth of 10 meters (Shevnina and Kourzeneva, 2017; Harris and Burton, 2010).

5.3 Model Limitation

The backscatter of LLOW is mainly disturbed by two types of factors: the first is external factors, such as wind speed and

440   direction, SAR image incidence angles, and mountain shadows; the other is the LLOW surface cover, such as floating ice and snow. Firstly, when the open water is disturbed by wind, the backscatter increases. Additionally, the incidence angles and topography also affect the backscatter of open water. Because the steep terrain yields mountain shadows and identification

errors (Dirscherl et al., 2021a), we calculated the slopes from DEM to evaluate the influence of topography. To evaluate the influence of wind, incidence angles, and topography, we sampled within the LLOW areas of four study areas from 2017 to
445 2021 from the 46 sample patches (Figs. S3, S4, S5, and S6). However, there is no obvious linear correlation between LLOW backscatter and wind, incidence angles or slope. What's more, we added the wind speed, incidence angles, and slope as input features for the RF model in open water identification. However, only incidence angle yields a significant feature importance. This indicates that the incidence angle is much more important for open water detection compared to wind speed and slope. Thus, our RF model did not consider the wind features and slope. Secondly, the unstable factors such as floating ice layers,
450 led to the fluctuations of the LLOW area. The backscatter of LLOW can be influenced by the floating ice layer and snow covering open water, making accurate identification challenging. By comparing our spatial errors with input SAR images, we found that the floating ice layers directly caused the false-positive errors (Fig. 8i). Furthermore, the presence of a blue ice layer with low backscatters can lead to overestimation of LLOW (Table S1). Despite our efforts to remove significantly underestimated results, as mentioned in Section 3.3, these factors remain the causes of fluctuations in the LLOW area series.

455 Although the LLOW identification model has these limitations, our findings demonstrate its strong performance across the four study areas. The deep learning approach, namely U-Net, enhanced model robustness across diverse environmental conditions such as various surrounding features, cloud covers, lighting conditions, and mountain shadows. Using the RF model to identify open water in SAR images can also overcome unstable factors such as cloud cover, producing the stable high-resolution time series of open water area. Therefore, our method has the potential to perform well in other regions, such as
460 identifying the other landlocked lakes in Antarctica or detecting numerous landlocked lakes along the coastal areas of Greenland. Additionally, our proposed method for distinguishing between seawater, supraglacial lakes, and landlocked lakes can be applied to the identification of thermokarst lakes, such as the numerous thermokarst lakes on the Alaskan North Slope. The BFS algorithm can distinguish between open rivers and closed lakes on plain permafrost. By utilizing BFS and the fusion of Landsat and Sentinel-1 images, we can differentiate thermokarst lakes and river drainages within an image. Consequently,
465 the growth of thermokarst lakes and their integration into river systems can also be detected. What's more, by combining Landsat and Sentinel-1 images, we overcame the severe cloud interference in the optical images in Antarctic, significantly improving the detection frequency of landlocked lakes. We also addressed the challenge of obtaining surrounding land cover information of water in SAR images, thereby successfully generated the high-resolution LLOW products. By providing reliable long-term LLOW series products, our model contributes to a deeper understanding of the dynamic changes of LLOW under a
470 changing climate.

6. Conclusion

We proposed an automated detection workflow for LLOW based on deep learning and multi-source satellite images. By utilizing the BFS algorithm and combining Landsat 8-9 OLI and Sentinel-1 SAR images, we successfully distinguished the

LLOW from other open waters, overcoming the limitation of models based solely on optical or SAR images. In our model accuracy assessment, our U-Net model and LLOW identification model achieved average F1 scores values of 0.90 and 0.89, respectively, on the testing datasets. Our model accurately recognizes both large-scale and small-scale LLOW in the testing images. Applying our LLOW identification model to four typical coastal Antarctic areas, we mitigated cloud and shadow interference and generated high-resolution spatiotemporal LLOW area time series from January to April between 2017 and 2021.

The seasonal changes in LLOW area can be categorized into two phases: the growth phase and the decline phase. The growth phase includes the period from the initiation of our data collection until reaching the maximum LLOW area, while the decline phase extends from the maximum area to the minimum area after reaching the peak. We found that during expansion of LLOW area, ~90% of the changes are explained by PDDs. PDDs can also influence the interannual variations in LLOW area, but the changes in PDD and LLOW area are not proportional. Furthermore, during the decline phase, NDDs accounted for more than 50% of changes in LLOW area. Our model provides long-term LLOW series products that help us better understand how lakes change under a changing climate.

Supplementary material

Please see the file of Supplementary material.

Data availability

Data presented in this work are in the process of being hosted on a public server by the Chinese National Arctic and Antarctic Data Center (https://www.chinare.org.cn/).

Author contribution

GS conceived the study. XM designed the method and provided model data. AJ analyzed the data and interpreted the results. AJ and XM designed and wrote the manuscript with the support of all co-authors. GS and YH improved the manuscript.

Competing interests

The authors declare no conflicts of interest relevant to this study.

Acknowledgements

This work was supported by the National Science Foundation of China (Grant Nos. 42276243 and 41922046 to GS; 42071306 to YH), and the Program of Shanghai Academic/Technology Research Leader (Grant No. 20XD1421600 to GS). The authors are grateful to CHINARE members for providing meteorological data.

References

Arthur, J. F., Stokes, C., Jamieson, S. S. R., Carr, J. R., and Leeson, A. A.: Recent understanding of Antarctic supraglacial lakes using satellite remote sensing, Prog. Phys. Geogr.: Earth Environ., 44, 837-869, https://doi.org/10.1177/0309133320916114, 2020.

Barrand, N. E., Vaughan, D. G., Steiner, N., Tedesco, M., Kuipers Munneke, P., van den Broeke, M. R., and Hosking, J. S.: Trends in Antarctic Peninsula surface melting conditions from observations and regional climate modeling, J. Geophys. Res.: Earth Surf., 118, 315-330, https://doi.org/https://doi.org/10.1029/2012JF002559, 2013.

Bowden, D., Clarke, A., Peck, L., and Barnes, D.: Antarctic sessile marine benthos: Colonisation and growth on artificial substrata over three years, Mar. Ecol. Prog. Ser., 316, 1-16, https://doi.org/10.3354/meps316001, 2006.

Braithwaite, R. J. and Hughes, P. D.: Positive degree-day sums in the Alps: a direct link between glacier melt and international climate policy, J. Glaciol., 68, 901-911, https://doi.org/10.1017/jog.2021.140, 2022.

Camacho, A.: Planktonic microbial assemblages and the potential effects of metazooplankton predation on the food web of lakes from the maritime Antarctica and sub-Antarctic islands, Rev. Environ. Sci. Biotechnol., 5, 167-185, https://doi.org/10.1007/s11157-006-0003-2, 2006.

Carvalho, F. R. S., Nastasi, F. R., Gamba, R. C., Foronda, A. S., and Pellizari, V. H.: Occurrence and Diversity of Legionellaceae in Polar Lakes of the Antarctic Peninsula, Curr. Microbiol., 57, 294-300, https://doi.org/10.1007/s00284-008-9192-y, 2008.

Convey, P. and Peck, L. S.: Antarctic environmental change and biological responses, Sci. Adv., 5, eaaz0888, https://doi.org/doi:10.1126/sciadv.aaz0888, 2019.

Ding, M., Zou, X., Sun, Q., Yang, D., Zhang, W., Bian, L., Lu, C., Allison, I., Heil, P., and Xiao, C.: The PANDA automatic weather station network between the coast and Dome A, East Antarctica, Earth Syst. Sci. Data, 14, 5019-5035, https://doi.org/10.5194/essd-14-5019-2022, 2022.

Dirscherl, M., Dietz, A. J., Kneisel, C., and Kuenzer, C.: Automated Mapping of Antarctic Supraglacial Lakes Using a Machine Learning Approach, Remote Sens., 12, 1203, 2020.

Dirscherl, M., Dietz, A. J., Kneisel, C., and Kuenzer, C.: A Novel Method for Automated Supraglacial Lake Mapping in Antarctica Using Sentinel-1 SAR Imagery and Deep Learning, Remote Sens., 13, https://doi.org/10.3390/rs13020197, 2021a.

Dirscherl, M., Dietz, A. J., Kneisel, C., and Kuenzer, C.: A Novel Method for Automated Supraglacial Lake Mapping in Antarctica Using Sentinel-1 SAR Imagery and Deep Learning, Remote Sens., 13, 197, 2021b.

Dirscherl, M. C., Dietz, A. J., and Kuenzer, C.: Seasonal evolution of Antarctic supraglacial lakes in 2015–2021 and links to environmental controls, The Cryosphere, 15, 5205-5226, https://doi.org/10.5194/tc-15-5205-2021, 2021c.

Fitzpatrick, A. A. W., Hubbard, A., Box, J. E., Quincey, D. J., As, D. v., Mikkelsen, A. B., Doyle, S. H., Dow, C. F., Hasholt, B., and Jones, G. A.: A decade (2002–2012) of supraglacial lake volume estimates across Russell Glacier, West Greenland, The Cryosphere, 8, 107-121, 2014.

Gorji, T., Yildirim, A., Hamzehpour, N., Tanik, A., and Sertel, E.: Soil salinity analysis of Urmia Lake Basin using Landsat-8 OLI and Sentinel-2A based spectral indices and electrical conductivity measurements, Ecol. Indic., 112, 106173, https://doi.org/https://doi.org/10.1016/j.ecolind.2020.106173, 2020.

Graf, R. and Tomczyk, A. M.: The Impact of Cumulative Negative Air Temperature Degree-Days on the Appearance of Ice Cover on a River in Relation to Atmospheric Circulation, Atmosphere, 9, 204, 2018.

Harris, U. and Burton, H.: Vestfold Hills Lake Bathymetry, Ver. 1 [dataset], 10.26179/5ce375c36a41c, 2010.

Hébert, M.-P., Beisner, B. E., Rautio, M., and Fussmann, G. F.: Warming winters in lakes: Later ice onset promotes consumer overwintering and shapes springtime planktonic food webs, Proc. Natl. Acad. Sci. U.S.A., 118,

e2114840118,https://doi.org/doi:10.1073/pnas.2114840118, 2021.

Hirose, T., Kapfer, M., Bennett, J., Cott, P., Manson, G., and Solomon, S.: Bottomfast Ice Mapping and the Measurement of
545 Ice Thickness on Tundra Lakes Using C-Band Synthetic Aperture Radar Remote Sensing1, JAWRA J. Am. Water Resour. Assoc., 44, 285-292,https://doi.org/https://doi.org/10.1111/j.1752-1688.2007.00161.x, 2008.

Hodgson, D. A.: Antarctic Lakes, in: Encyclopedia of Lakes and Reservoirs, edited by: Bengtsson, L., Herschy, R. W., and Fairbridge, R. W., Springer, Netherlands, 26-31, 10.1007/978-1-4020-4410-6_38, 2012.

Huang, J. P., Swain, A. K., Andersen, D. T., and Bej, A. K.: Bacterial diversity within five unexplored freshwater lakes
550 interconnected by surface channels in East Antarctic Dronning Maud Land (Schirmacher Oasis) using amplicon pyrosequencing, Polar Biol., 37, 359-366,https://doi.org/10.1007/s00300-013-1436-z, 2014.

Huang, Z., Wu, W., Liu, H., Zhang, W., and Hu, J.: Identifying Dynamic Changes in Water Surface Using Sentinel-1 Data Based on Genetic Algorithm and Machine Learning Techniques, Remote Sens., 13,https://doi.org/10.3390/rs13183745, 2021.

Izaguirre, I., Allende, L., and Romina Schiaffino, M.: Phytoplankton in Antarctic lakes: biodiversity and main ecological
555 features, Hydrobiologia, 848, 177-207,https://doi.org/10.1007/s10750-020-04306-x, 2021.

Johansson, A. M. and Brown, I. A.: Adaptive Classification of Supra-Glacial Lakes on the West Greenland Ice Sheet, IEEE J. Sel. Top. Appl. Earth Obs. Remote Sens., 6, 1998-2007,https://doi.org/10.1109/JSTARS.2012.2233722, 2013.

Johansson, A. M., Jansson, P., and Brown, I. A.: Spatial and temporal variations in lakes on the Greenland Ice Sheet, J. Hydrol., 476, 314-320, 2013.

560 Keskitalo, J., Leppäranta, M., and Arvola, L.: First records of primary producers of epiglacial and supraglacial lakes in western Dronning Maud Land, Antarctica, Polar Biol., 36, 1441-1450,https://doi.org/10.1007/s00300-013-1362-0, 2013.

Kirillin, G., Leppäranta, M., Terzhevik, A., Granin, N., Bernhardt, J., Engelhardt, C., Efremova, T., Golosov, S., Palshin, N., Sherstyankin, P., Zdorovennova, G., and Zdorovennov, R.: Physics of seasonally ice-covered lakes: a review, Aquat. Sci., 74, 659-682,https://doi.org/10.1007/s00027-012-0279-y, 2012.

565 Komárek, J., Nedbalová, L., and Hauer, T.: Phylogenetic position and taxonomy of three heterocytous cyanobacteria dominating the littoral of deglaciated lakes, James Ross Island, Antarctica, Polar Biol., 35, 759-774,https://doi.org/10.1007/s00300-011-1123-x, 2012.

Koo, H., Ptacek, T., Crowley, M., Swain, A. K., Osborne, J. D., Bej, A. K., and Andersen, D. T.: Draft Genome Sequence of Hymenobacter sp. Strain IS2118, Isolated from a Freshwater Lake in Schirmacher Oasis, Antarctica, Reveals Diverse Genes
570 for Adaptation to Cold Ecosystems, Genome Announc., 2, e00739-00714,https://doi.org/10.1128/genomeA.00739-14, 2014.

Lazhu, Yang, K., Hou, J., Wang, J., Lei, Y., Zhu, L., Chen, Y., Wang, M., and He, X.: A new finding on the prevalence of rapid water warming during lake ice melting on the Tibetan Plateau, Sci. Bull., 66, 2358-2361,https://doi.org/https://doi.org/10.1016/j.scib.2021.07.022, 2021.

Lecomte, K. L., A. Vignoni, P., Córdoba, F. E., Chaparro, M. A. E., Chaparro, M. A. E., Kopalová, K., Gargiulo, J. D., M. Lirio,
575 J., Irurzun, M. A., and Böhnel, H. N.: Hydrological systems from the Antarctic Peninsula under climate change: James Ross archipelago as study case, Environ. Earth Sci., 75, 623,https://doi.org/10.1007/s12665-016-5406-y, 2016.

Leeson, A. A., Shepherd, A., Briggs, K., Howat, I., Fettweis, X., Morlighem, M., and Rignot, E.: Supraglacial lakes on the Greenland ice sheet advance inland under warming climate, Nat. Clim. Change, 5, 51-55,https://doi.org/10.1038/nclimate2463, 2015.

580 Li Qing, Z. C., Liu Ruixi, Zheng Lei: Monitoring the changes of supraglacial lakes on the Polar Record Glacier, East Antarctic, Chin. J. Polar Res., 33(1), 27-36, 2021.

Liang, D., Guo, H., Zhang, L., Cheng, Y., Zhu, Q., and Liu, X.: Time-series snowmelt detection over the Antarctic using Sentinel-1 SAR images on Google Earth Engine, Remote Sens. Environ., 256, 112318,https://doi.org/https://doi.org/10.1016/j.rse.2021.112318, 2021.

585 Liang, J. and Liu, D.: A local thresholding approach to flood water delineation using Sentinel-1 SAR imagery, ISPRS J. Photogramm. Remote Sens., 159, 53-62,https://doi.org/https://doi.org/10.1016/j.isprsjprs.2019.10.017, 2020.

Lyons, W. B., Laybourn-Parry, J., Welch, K. A., and Priscu, J. C.: Antarctic Lake Systems and Climate Change, in: Trends in Antarctic Terrestrial and Limnetic Ecosystems: Antarctica as a Global Indicator, edited by: Bergstrom, D. M., Convey, P., and Huiskes, A. H. L., Springer Netherlands, Dordrecht, 273-295, 10.1007/1-4020-5277-4_13, 2006.

590 Maisincho, L., Favier, V., Wagnon, P., Basantes Serrano, R., Francou, B., Villacis, M., Rabatel, A., Mourre, L., Jomelli, V., and Cáceres, B.: On the interest of positive degree day models for mass balance modeling in the inner tropics, The Cryosphere Discuss., 2014, 2637-2684,https://doi.org/10.5194/tcd-8-2637-2014, 2014.

Miles, K. E., Willis, I. C., Benedek, C. L., Williamson, A. G., and Tedesco, M.: Toward Monitoring Surface and Subsurface Lakes on the Greenland Ice Sheet Using Sentinel-1 SAR and Landsat-8 OLI Imagery, Front. Earth Sci., 5,https://doi.org/10.3389/feart.2017.00058, 2017.

Moussavi, M., Pope, A., Halberstadt, A. R. W., Trusel, L. D., Cioffi, L., and Abdalat, W.: Antarctic supraglacial lake detection using landsat 8 and sentinel-2 imagery: Towards continental generation of lake volumes, Remote Sens., 12, 134,https://doi.org/10.3390/RS12010134, 2020.

Muñoz Sabater, J.: ERA5-Land monthly averaged data from 1950 to present [dataset], 10.24381/cds.68d2bb30, 2019.

Papale, M., Rizzo, C., Villescusa, J. A., Rochera, C., Camacho, A., Michaud, L., and Lo Giudice, A.: Prokaryotic assemblages in the maritime Antarctic Lake Limnopolar (Byers Peninsula, South Shetland Islands), Extremophiles, 21, 947-961,https://doi.org/10.1007/s00792-017-0955-x, 2017.

Parnikoza, I. and Kozeretska, I. A.: Antarctic Terrestrial Biome—Most Poor, Extreme and Sensitive on the Planet,

Pöysä, H.: Local variation in the timing and advancement of lake ice breakup and impacts on settling dynamics in a migratory waterbird, Sci. Total Environ., 811, 151397,https://doi.org/https://doi.org/10.1016/j.scitotenv.2021.151397, 2022.

Prater, C., Bullard, J. E., Osburn, C. L., Martin, S. L., Watts, M. J., and Anderson, N. J.: Landscape Controls on Nutrient Stoichiometry Regulate Lake Primary Production at the Margin of the Greenland Ice Sheet, Ecosystems, 25, 931-947,https://doi.org/10.1007/s10021-021-00693-x, 2022.

Preston, D. L., Caine, N., McKnight, D. M., Williams, M. W., Hell, K., Miller, M. P., Hart, S. J., and Johnson, P. T.: Climate regulates alpine lake ice cover phenology and aquatic ecosystem structure, Geophys. Res. Lett., 43, 5353-5360,https://doi.org/10.1002/2016GL069036, 2016.

Prowse, T., Alfredsen, K., Beltaos, S., Bonsal, B. R., Bowden, W. B., Duguay, C. R., Korhola, A., McNamara, J., Vincent, W. F., Vuglinsky, V., Anthony, K. M. W., and Weyhenmeyer, G. A.: Effects of Changes in Arctic Lake and River Ice, AMBIO, 40, 63-74,https://doi.org/10.1007/s13280-011-0217-6, 2011.

Quayle Wendy, C., Peck Lloyd, S., Peat, H., Ellis-Evans, J. C., and Harrigan, P. R.: Extreme Responses to Climate Change in Antarctic Lakes, Science, 295, 645,https://doi.org/10.1126/science.1064074, 2002.

Rochera, C. and Camacho, A.: Limnology and Aquatic Microbial Ecology of Byers Peninsula: A Main Freshwater Biodiversity Hotspot in Maritime Antarctica, Diversity, 11, 201, 2019.

Roman, M., Nedbalová, L., Kohler, T. J., Lirio, J. M., Coria, S. H., Kopáček, J., Vignoni, P. A., Kopalová, K., Lecomte, K. L., Elster, J., and Nývlt, D.: Lacustrine systems of Clearwater Mesa (James Ross Island, north-eastern Antarctic Peninsula): geomorphological setting and limnological characterization, Antarct. Sci., 31, 169-188,https://doi.org/10.1017/S0954102019000178, 2019.

Ronneberger, O., Fischer, P., and Brox, T.: U-Net: Convolutional Networks for Biomedical Image Segmentation, Cham, 234-241, 10.1007/978-3-319-24574-4_28,

Seppelt, R. D. and Broady, P. A.: Antarctic terrestrial ecosystems: The Vestfold Hills in context, Hydrobiologia, 165, 177-184,https://doi.org/10.1007/BF00025586, 1988.

Shevnina, E. and Kourzeneva, E.: Thermal regime and components of water balance of lakes in Antarctica at the Fildes peninsula and the Larsemann Hills, Tellus A: Dyn. Meteorol. Oceanogr., 69, 1317202,https://doi.org/10.1080/16000870.2017.1317202, 2017.

Shevnina, E., Kourzeneva, E., Dvornikov, Y., and Fedorova, I.: Retention time of lakes in the Larsemann Hills oasis, East Antarctica, The cryosphere, 15, 2667-2682,https://doi.org/10.5194/tc-15-2667-2021, 2021.

Shi, G., Teng, J., Ma, H., Wang, D., and Li, Y.: Metals in topsoil in Larsemann Hills, an ice-free area in East Antarctica: Lithological and anthropogenic inputs, CATENA, 160, 41-49,https://doi.org/https://doi.org/10.1016/j.catena.2017.09.001, 2018.

Shokr, M. and Dabboor, M.: Observations of SAR polarimetric parameters of lake and fast sea ice during the early growth phase, Remote Sens. Environ., 247, 111910,https://doi.org/https://doi.org/10.1016/j.rse.2020.111910, 2020.

Siddique, N., Paheding, S., Elkin, C. P., and Devabhaktuni, V.: U-Net and Its Variants for Medical Image Segmentation: A Review of Theory and Applications, IEEE Access, 9, 82031-82057,https://doi.org/10.1109/ACCESS.2021.3086020, 2021.

Silvela, J. and Portillo, J.: Breadth-first search and its application to image processing problems, IEEE Trans. Image Process., 10, 1194-1199,https://doi.org/10.1109/83.935035, 2001.

Srivastava, A. K., Randive, K. R., and Khare, N.: Mineralogical and geochemical studies of glacial sediments from Schirmacher Oasis, East Antarctica, Quat. Int., 292, 205-216,https://doi.org/https://doi.org/10.1016/j.quaint.2012.07.028, 2013.

Stokes, C. R., Sanderson, J. E., Miles, B. W. J., Jamieson, S. S. R., and Leeson, A. A.: Widespread distribution of supraglacial lakes around the margin of the East Antarctic Ice Sheet, Sci. Rep., 9, 13823,https://doi.org/10.1038/s41598-019-50343-5, 2019.

645 Taton, A., Grubisic, S., Balthasart, P., Hodgson, D. A., Laybourn-Parry, J., and Wilmotte, A.: Biogeographical distribution and ecological ranges of benthic cyanobacteria in East Antarctic lakes, FEMS Microbiol. Ecol., 57, 272-289,https://doi.org/10.1111/j.1574-6941.2006.00110.x, 2006.

Turner, J., Lu, H., White, I., King, J. C., Phillips, T., Hosking, J. S., Bracegirdle, T. J., Marshall, G. J., Mulvaney, R., and Deb, P.: Absence of 21st century warming on Antarctic Peninsula consistent with natural variability, Nature, 535, 411-

650 415,https://doi.org/10.1038/nature18645, 2016.

Villaescusa, J. A., Jørgensen, S. E., Rochera, C., Velázquez, D., Quesada, A., and Camacho, A.: Carbon dynamics modelization and biological community sensitivity to temperature in an oligotrophic freshwater Antarctic lake, Ecol. Modell., 319, 21-30,https://doi.org/https://doi.org/10.1016/j.ecolmodel.2015.03.008, 2016.

Wakabayashi, H., Motohashi, K., and Maezawa, N.: Monitoring Lake Ice in Northern Alaska with Backscattering and

655 Interferometric Approaches Using Sentinel-1 Sar Data, 2019, 4202-4205, 10.1109/IGARSS.2019.8900371,

Wake, L. and Marshall, S.: Assessment of current methods of positive degree-day calculation using in situ observations from glaciated regions, J. Glaciol., 61, 329-344,https://doi.org/10.3189/2015JoG14J116, 2015.

Wangchuk, S., Bolch, T., and Zawadzki, J.: Towards automated mapping and monitoring of potentially dangerous glacial lakes in Bhutan Himalaya using Sentinel-1 Synthetic Aperture Radar data, Int. J. Remote Sens., 40, 4642-

660 4667,https://doi.org/10.1080/01431161.2019.1569789, 2019.

Wu, B., Fang, Y., and Lai, X.: Left ventricle automatic segmentation in cardiac MRI using a combined CNN and U-net approach, Comput. Med. Imaging Graphics, 82, 101719,https://doi.org/https://doi.org/10.1016/j.compmedimag.2020.101719, 2020.

Yang, F., Cen, R., Feng, W., Zhu, Q., Leppäranta, M., Yang, Y., Wang, X., and Liao, H.: Dynamic simulation of nutrient

665 distribution in lakes during ice cover growth and ablation, Chemosphere, 281, 130781,https://doi.org/https://doi.org/10.1016/j.chemosphere.2021.130781, 2021.

Zakhvatkina, N., Smirnov, V., and Bychkova, I.: Satellite SAR Data-based Sea Ice Classification: An Overview, Geosciences, 9, 152,https://doi.org/10.3390/geosciences9040152, 2019.

670